Materials Today Bio 35 (2025) 102281

Contents lists available at ScienceDirect

Materials Today Bio

journal homepage: www.journals.elsevier.com/materials-today-bio

Light-induced field effect transistor-based biosensor consisted of aptamer and ReS_2 single crystal layer for exosome detection

Moonbong Jang [a,1], Woongki Na [b,1], Minyoung Lee [a,1], Seokho Jung [a], Yeeun Woo [a], Hah Young Yoo [c], Taek Lee [a,*], Junhong Min [d,**]

[a] Department of Chemical Engineering, Kwangwoon University, 20 Gwangwoon-Ro, Nowon Gu, Seoul, 01897, Republic of Korea
[b] Department of Physics, Sogang University, 35 Baekbeom-ro, Mapo-gu, Seoul, 04107, Republic of Korea
[c] Department of Biotechnology, Sangmyung University, 20, Hongjimun 2-Gil, Jongno-gu, Seoul, 03016, Republic of Korea
[d] School of Integrative Engineering, Chung-Ang University, 84 Heukseok-Ro, Dongjak-Gu, Seoul, 06974, Republic of Korea

ARTICLE INFO

Keywords:
Light-induced FET
Biosensor
Exosome detection
Single-crystal ReS_2
Diagnostic technology
Photo-generated carrier

ABSTRACT

Field-effect transistor (FET)-based biosensors are promising platforms for point-of-care diagnostics because of their low power requirements, miniaturization capabilities, and high sensitivity toward charged biomolecules. In particular, light-induced FET (L-FET) facilitate photo-generated carrier signal amplification using an external light source, enabling high detection sensitivity from minimal sample volumes. This study proposed the first L-FET biosensor that integrated single-crystal ReS_2 with biomolecules to achieve effective photo-generated carrier signal amplification. ReS_2 maintains its single-layer electronic characteristics even in bulk, thus minimizing signal variability across devices. The ReS_2 current channel is established via mechanical exfoliation onto Au electrodes on a SiO_2 substrate, and photo-generated carrier amplification was induced using a photoconductive effect via laser illumination. Signal variation was assessed using 2-channel I-V measurements following the biomolecular complex formation. The results demonstrated an approximately two times increase in the photo-generated carrier amplification ratio. The detection range for exosomes targeting CD9 protein within human serum was determined to be 10^2–10^7 exosomes/mL, with a limit of detection (LOD) of 9.79×10^3 exosomes/mL, thereby demonstrating stable detection even at low concentrations. The proposed L-FET biosensor design which incorporated direct bioconjugation with semiconductor devices offered a fundamental advance for early diagnostic platforms. The device's simplified architecture and signal amplification mechanism exhibited advantages for large-scale production, enhancing its commercial viability, and highlighting its potential to impact the evolution of next-generation medical diagnostic technologies enormously. This study introduced a new paradigm for FET-based biosensors, positioning this platform as a candidate for diverse biomarker detection and early disease diagnostic applications.

1. Introduction

The development of cancer is a prolonged and insidious process, progressing silently within the tissue, yet it persistently leaves molecular footprints beyond the cellular boundary. In particularly, exosomes ranging from 30–200 nm in diameter, carry metabolites and genetic materials derived from their parent cells [1,2]. Their molecular composition exhibits notable alterations from the earliest stages of disease progression. Tetraspanin family surface proteins have been extensively utilized as potential biomarkers for cancer-associated exosomes [3,4]. Notably, cluster of differentiation 9 (CD9) has been implicated in pancreatic cancer through multiple studies [5], serving both as a biological indicator linked to tumor invasiveness and prognosis, and as a promising target for early detection. According to the World Health Organization (WHO), the ideal method for detecting disease or external pathogens should be rapid, sensitive, simple, and

This article is part of a special issue entitled: Multiscale Composites published in Materials Today Bio.

* Corresponding author. Department of Chemical Engineering, Kwangwoon University, Seoul, Republic of Korea.
** Corresponding author. School of Integrative Engineering, Chung-Ang University, Seoul, Republic of Korea.
E-mail addresses: bong1998@kw.ac.kr (M. Jang), woongki@sogang.ac.kr (W. Na), dalsdud005@kw.ac.kr (M. Lee), jsh990425@kw.ac.kr (S. Jung), yenn0706@kw.ac.kr (Y. Woo), y2h2000@smu.ac.kr (H.Y. Yoo), tlee@kw.ac.kr (T. Lee), junmin@cau.ac.kr (J. Min).
[1] These authors contributed equally.

https://doi.org/10.1016/j.mtbio.2025.102281
Received 16 June 2025; Received in revised form 20 August 2025; Accepted 2 September 2025
Available online 8 September 2025
2590-0064/© 2025 The Authors. Published by Elsevier Ltd. This is an open access article under the CC BY-NC license (http://creativecommons.org/licenses/by-nc/4.0/).

cost-effective, guiding the development and application of diagnostic technologies [6]. Currently, healthcare professionals use various diagnostic methods to accurately interpret viral exposure and immune responses including medical imaging technologies [7], immunochromatography [8], polymerase chain reaction (PCR) tests [9], and biopsies [10]. Medical imaging plays a pivotal role in clinical decision-making by focusing on the precise visualization of structures for specific diagnostic purposes. Other techniques offer the advantage of diagnoses with minimal sample volumes while maintaining high detection sensitivity. However, traditional diagnostic technologies require highly skilled professionals [11], sophisticated equipment [12], considerable time [13], and enormous expense [14], making them unsuitable for point-of-care or early diagnosis applications. Consequently, addressing these limitations remains a challenge.

Medical associations have recently shifted toward using biosensors that can offer cost-effective, quick, and simple diagnostic evaluations [15]. Such biosensors enable the real-time observation of specific interactions through a combination of various biological receptors such as antibodies, enzymes, proteins, and nucleic acids with physicochemical transducers [16]. To facilitate rapid point-of-care diagnostics by non-specialists without the need for centralized hospital visits, numerous studies have focused on developing compact and easy-to-use structures [17–20]. Among these, field-effect transistor (FET)-based biosensors have garnered considerable attention as promising alternatives for point-of-care diagnostics, demonstrating high detection capabilities and sensitivity to both neutral and charged biomolecules [21]. Their low operating power and potential for miniaturization further enhance their suitability for such applications [22]. The incorporation of nanomaterials into FET sensors which can enhance their sensitivity offers advantageous structures for biomolecule detection owing to their high surface-to-volume ratio [23]. However, signal variability between devices fabricated within the same production batch and bandgap changes caused by variations in thickness can pose major commercialization challenges [24]. Thus, structural modifications capable of delivering consistently high performance across a broad spectral range are required to overcome these limitations.

Transition metal dichalcogenide (TMD) ReS_2 serves as a channel material that offers stability and excellent performance owing to its mechanical flexibility and high carrier mobility [25]. It forms a two-dimensional structure with a transition metal layer sandwiched between chalcogen layers [26], allowing for the versatile tuning of electronic properties under incident light, which is advantageous for the development of various biosensors [27]. Although other TMD materials exhibit high electron mobility and thermal conductivity only in 2D limits [28,29], ReS_2 maintains its independent characteristics regardless of the number of layers as inter-layer interaction of the system is known to be relatively weak [30]. Moreover, rhenium disulfide (ReS_2) exhibits high sensitivity to the surrounding polarity, providing superior detection capabilities compared to conventional three-dimensional channel structures. In particular, it maintains a direct bandgap of approximately 1.5 eV from the bulk form to a single layer, thereby ensuring high charge mobility and photosensitivity [31]. This characteristic minimizes the device-to-device variability and enables efficient photodetection.

ReS_2-based light-induced field-effect transistor (L-FET) offers unique physical mechanisms that can amplify the benefits of conventional FET structures [32]. The photoconductive effect (PCE), which occurs when semiconductor carriers are enhanced by photon energy exceeding the bandgap, quantitatively increases carrier concentration and conductivity [33]. The direct bandgap of ReS_2 is favorable for the PCE, allowing substantial signal amplification. Moreover, L-FET presents an innovative structural advantage by enhancing the detection performance through a simplified design and, eliminating the complex gate and oxide structures typical of FETs. Rather than relying on the gate voltage to control the channel current, the L-FET employs light to stimulate the PCE, thereby increasing the charge carrier concentration and realizing a simple structure. Although much research has focused on developing devices that integrate direct circuitry with biological mediators [34–37], a model that combines a light-driven FET architecture with the direct immobilization of biomolecules onto a 2D semiconducting channel has not yet been demonstrated.

In this study, we proposed an L-FET-based biosensor comprising a single-crystal ReS_2 layer functionalized with a CD9 aptamer, designed to detect exosomes through the CD9 protein. Organic acceptors and target proteins were deposited using a droplet method, forming a robust and reproducible interface with the ReS_2 surface. By applying incident light, photo-generated carriers are generated via the PCE, which enhances I_{ds}, resulting in a highly sensitive detection signal [38]. The I_{ds} refers to the electrical current flowing between two gold electrodes—the source and drain—via a two-dimensional ReS_2 channel. This channel–electrode structure is fabricated on a SiO_2 insulating substrate. The incident light was designed to replace the gate and oxide layers, simplifying the conventional FET structure, as illustrated in Fig. 1. Additionally, by introducing ReS_2 as the channel material, we ensured that the physical properties of the monolayer were preserved even in multilayer configurations, minimizing signal variation between devices. Notably, this structural approach facilitates scalable sensor integration while preserving the intrinsic optoelectronic properties of ReS_2. The sensing structure could then be integrated directly with the ReS_2 channel, and measurements could be conducted under conditions that prevented damage to biomolecules [39].

In the designed L-FET, the channel current amplification ratio due to induced photogenerated carriers under incident light exhibited an approximately two times increase, confirming substantial signal amplification. Notably, meaningful photo-generated carrier signal amplification was evident even at a low illumination power level of approximately 400 μW. Moreover, in a simulated clinical evaluation conducted in 10 % human serum, the limit of detection (LOD) for exosomes was determined to be 9.79×10^3 exosomes/mL, demonstrating comparable performance to previously reported biosensors with similar FET-based structures [40]. This demonstrated that sensitive detection was achievable with small sample volumes through photo-generated carrier signal amplification. The proposed sensor design, combining fabrication simplicity with robust performance, holds potential for commercialization as a broadly applicable diagnostic platform.

2. Materials and methods

2.1. Materials

The monochromator, spectrograph, and 50 × long working distance objective lens (NA: 0.5) were purchased from DXG (Gangnam, South Korea). The filter holder (FH2), optical density 1.0 ND filter (NE210B), optical density 0.4 ND filter (NE204B), power meter (PM16-130), optical posts (TR50, TR150), post holder (PH20), and heavy-duty switchable magnetic base (MB175) were obtained from Thorlabs (Jersey, USA). ReS_2 single crystals and MoS_2 single crystals were sourced from Uni Nanotech (Yongin, South Korea), whereas the 2D_high positioner (PB100) for ReS_2 transfer was acquired from MS TECH (Suwon, South Korea). The SYLGARD 184 Silicone Elastomer kit used for fabricating polydimethylsiloxane (PDMS) was purchased from Indmall (Sungnam, South Korea). The DNA sequence that is specifically bound to the CD9 protein was adopted from a previous study and used as a bioprobe [41]. The aptamer sequence (5′-ATA GTC CCT TGG CGT GCT TCA CAA CCT TGA ACT TGA CGC AGG ATC GTT CAG TGC GCA CTA GAG CAG GTA CGG TGT CA-3) was synthesized with a thiol group at the 5′- end by Bionics (Seoul, South Korea). CD9 protein was purchased from Sino Biological (Beijing, China). Human serum was obtained from Sigma-Aldrich (St. Louis, MO, USA), and human preadipocyte exosomes were purchased from Zenbio (Durham, USA). Au microgap electrodes were fabricated at the Korea Nanotechnology Research Center (Daejeon, South Korea). Acetone (ACE; C_3H_6O) and ethyl alcohol (ETOH; C_2H_5OH) were purchased from Daejung (Siheung, South Korea).

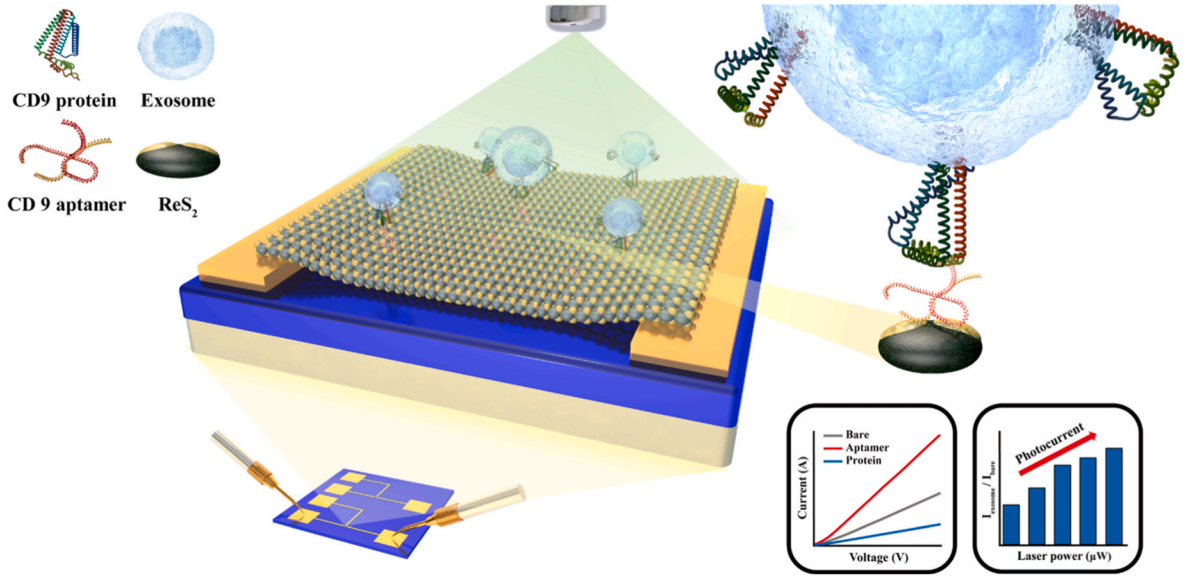


Fig. 1. Schematic illustration of the fabricated L-FET platform.

2.2. Fabrication of L-FET device using Au micro-gap electrode

A specially designed Au-gap electrode was prepared. This electrode was designed for convenience in observing optical properties by applying single-crystal ReS_2 between the Au microgap, and it has sufficient space for irradiating a laser light source. The Au microgap electrode was manufactured by SNI Technology (Gyeonggido, Korea) [40,44]. Detailed information regarding the manufactured L-FET is shown in Fig. S1. Cr (2 nm) and Au (50 nm) were deposited on the electrode surface using a SiO_2 substrate via an electron beam evaporator. The electrodes had a square design of 1 cm^2. The CAD design of the Au electrodes used in this study, along with actual images of the fabricated electrodes, are presented in Fig. S1a and S1b. The electrodes formed a microgap approximately 10 μm in width, as shown in the magnified view in Fig. S1c.

2.3. Fabrication and functionalization of ReS_2-based FET device for CD9 protein sensing

The ReS_2-based FET device was fabricated by mechanically exfoliating single-crystal ReS_2 into few-layer flakes, which were initially transferred onto a PDMS film serving as a transfer medium. The PDMS, prepared by mixing the elastomer base and curing agent in a 9:1 ratio and curing at 75 °C for 24 h, was formed into a thin film to enable precise transfer. To employ single-crystal flakes, ReS_2 thickness on the PDMS substrate was assessed to be sufficiently thin, as confirmed by optical microscopy. The optical contrast between the flakes and the underlying substrate served as a reliable criterion for thickness evaluation. Samples exhibiting a distinct color variation relative to bulk ReS_2 were subsequently selected for experimental investigation. To construct the sensing structure, Au electrodes were sonicated for 5 min in an ultrasonic cleaner (DAIHAN Scientific, Daegu, South Korea) with acetone (ACE), followed by washing with ethanol (ETOH) and deionized water (DIW). The residual solution on the substrate was dried using N_2 gas. To achieve precise placement of single-crystalline ReS_2 within the microgap region, a microscope mounted on an atomic force microscope (AFM) was employed. The pre-cleaned electrode was first mounted securely onto the designated position of the AFM stage. Subsequently, a PDMS carrying the selected ReS_2 flake was positioned on an additional slide glass system, with the adhesive side facing downward. Due to its inherent self-adhesive nature, the PDMS remained stably affixed without displacement caused by gravity. Focus adjustment and alignment were performed using the AFM software, followed by fine-tuning of the Z-axis translation stage to ensure accurate contact between the ReS_2 flake and the electrode gap. Gradual peeling of the PDMS layer mitigates shear stress, enabling uniform transfer of the TMD film onto the substrate [55]. This process enhances both the mechanical integrity of the film and the overall transfer yield. The transfer procedure was conducted under real-time monitoring, allowing for the reliable and accurate placement of the single-crystal ReS_2 at the target site between the electrodes. To achieve self-assembly, 10 μL of the SH-modified CD9 aptamer was applied to the formed ReS_2 channel. The thiol-modified CD9 aptamer (SH-CD9 aptamer) self-assembles onto the ReS_2 surface via its terminal thiol group (–SH). This is based on covalent interactions—such as S–S bonding or S–Re–S coordination—occurring at sulfur atoms or defect sites, and naturally binds to the layered structure of the ReS_2 surface without requiring additional binding agents. Building on this theoretical rationale, aptamers were deposited onto the ReS_2 surface via drop-casting and allowed to react at room temperature for 3 h to achieve immobilization. Stable attachment was confirmed even after rinsing with DIW. The preadipocyte exosomes were then diluted and reacted at room temperature for 3 h to facilitate the binding of the target molecule, CD9 protein. Following each reaction, the samples were rinsed with DIW and dried at room temperature to minimize damage to the ReS_2 channel and the biomolecules.

2.4. Application of incident light for inducing the photoconductive effect

The single-crystal ReS_2 was deposited onto the Au microgap electrodes, with the sensing structure subsequently immobilized on the channel surface in the following order: bare, SH-CD9 aptamer, and preadipocyte exosome. Laser irradiation was then applied in a configuration designed to facilitate variations in optical power, as illustrated in Fig. S1d. Fig. S1e shows the configuration in which the position-adjustment devices were placed at the source and drain of the electrode to enable current measurements under laser illumination, the laser is aligned with the center of the channel prior to measurements, as shown in Fig. S1f. To optimize the PCE, the optical power was adjusted incrementally, reaching a peak of 3 mW using a 50 × long working distance objective lens (NA: 0.5).

2.5. Surface characterization of transferred ReS_2 channels and sensing structures on Au microgap

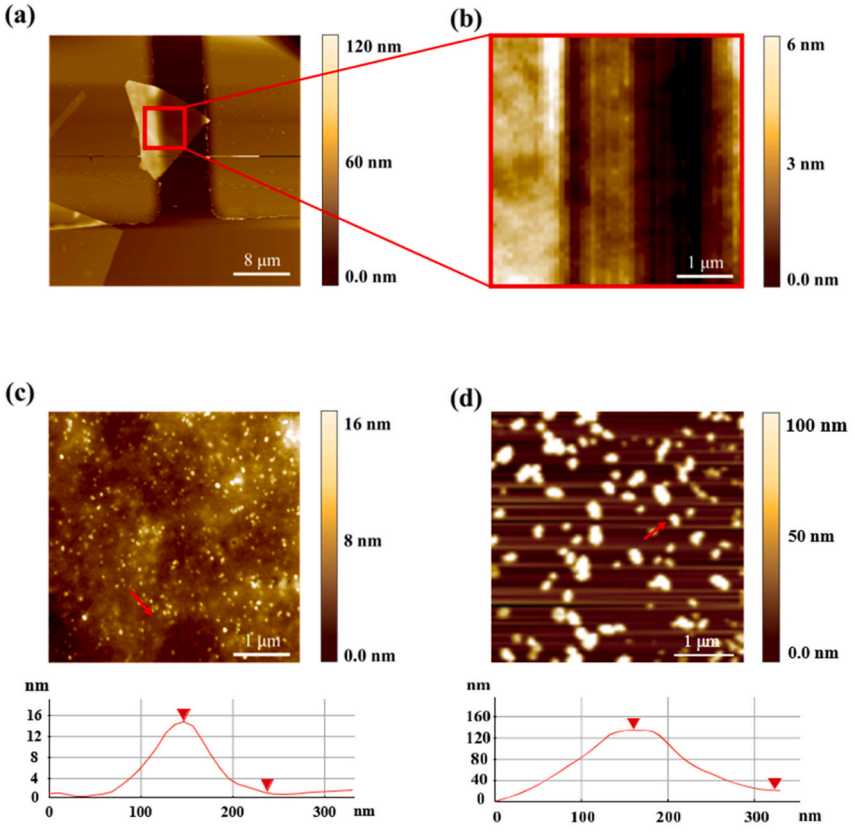
The surface information of the ReS_2 channel transferred to the Au microgap and the surface characteristics at each deposition step of the sensing structure were analyzed using an AFM (XE7, Park Systems, Suwon, South Korea). The cantilever used for the surface measurements was a PPP-NCHR equipped with a silicon tip with a resonant frequency of 330 kHz and spring constant of 40 N/m (Park Systems, Suwon, South Korea). The operating conditions such as the scan rate, set point, Z-gain, and Z-height were adjusted in real-time based on the varying surface conditions of the samples at different positions.

3. Results and discussion

3.1. Analysis of stepwise biomolecule immobilization on ReS_2 channel surface

First, to validate the structural integrity and functionalization of the ReS_2-based biosensor, we used AFM to analyze each stage of biomolecule immobilization on the ReS_2 channel. AFM provides detailed insights into the surface characteristics and vertical distance at each immobilization step, which are crucial for confirming the successful construction of the sensing structure. This section presents AFM data that visually and quantitatively corroborate the formation of a stable biosensing interface, which is essential for achieving consistent detection performance in L-FET-based sensors.

The thiol-functionalized CD9 aptamer (SH-CD9 Aptamer) naturally binds to the layered structure of the ReS_2 surface when provided with sufficient binding time, without requiring additional binding agents [41]. Consequently, immobilization can be accomplished by the direct exposure of channel [42]. Accordingly, the sensing structure was established by targeting the CD9 protein present in adipocyte exosomes. Previous studies have reported that immobilized aptamers can directly detect the CD9 protein, a surface marker of exosomes. Therefore, in this study, adipocyte-derived exosomes were employed instead of using the CD9 protein itself to facilitate binding. Surface characterization at each immobilization step was conducted using AFM (Fig. 2a–d). Fig. 2a illustrates the bare surface of the transferred ReS_2 within the microgap of the Au electrode, reflecting the physical characteristics of the thinned flake produced through mechanical exfoliation. Owing to the non-uniform exfoliation force applied across the flakes, the number of layers varied in different regions. This variability was further corroborated by the optical microscopy and AFM surface data, as shown in



(e)

	ReS_2	ReS_2/CD9 aptamer	ReS_2/aptamer/exosome
Vertical Distance (nm)	3.762 ± 0.670	14.005 ± 0.161	109.76 ± 3.035
RMS Roughness (Rq) (nm)	1.029 ± 0.169	4.029 ± 0.522	40.788 ± 0.564
Roughness Average (Ra) (nm)	0.870 ± 0.172	3.278 ± 0.675	37.366 ± 0.488

Fig. 2. Surface analysis of the ReS_2 channel via AFM. (a) AFM image of the ReS_2 channel deposited between Au electrodes. (b) AFM image showing a magnified view of the red square-marked region on the surface of the ReS_2 channel. The step height variation due to differences in layers is observed. (c) AFM image showing aptamers conjugated to the ReS_2 surface through -SH groups. (d) AFM image of exosomes derived from adipocytes bound to the aptamers. (e) Summary of surface analysis using AFM images. (For interpretation of the references to color in this figure legend, the reader is referred to the Web version of this article.)

Fig. S2a and S2b, which depict the step height differences across distinct locations (Fig. 2b). Following aptamer immobilization, the vertical distance increased by approximately 14 nm. The binding of the SH-functionalized aptamer to ReS_2 resulted in localized height increases, although the height distribution was not uniform across the flakes. This could be attributed to the structural stability of ReS_2 over a relatively broad surface area, which led to considerable aptamer aggregation in specific stable regions. Additionally, the observed height variation following the immobilization of the 77 bp CD9 aptamer is considered to result from a combination of its intrinsic three-dimensional folding and surface interactions occurring under the immobilization conditions [43] (Fig. 2c). Fig. 2d illustrates the AFM image of adipocyte-derived exosomes bound to the aptamer-functionalized electrode. The image reveals a considerable increase in vertical distance, measuring approximately 95 nm, across the ReS_2 surface, along with irregularly immobilized elliptical particles. These images were consistent with the morphology of exosomes reported in previous studies, suggesting two possible explanations. First, the CD9 protein, a surface marker of exosomes, may not be uniformly distributed or quantitatively consistent across the particles, leading to heterogeneous binding. Second, the interaction between the exosomes and the aptamer may result in the observed irregular binding patterns.

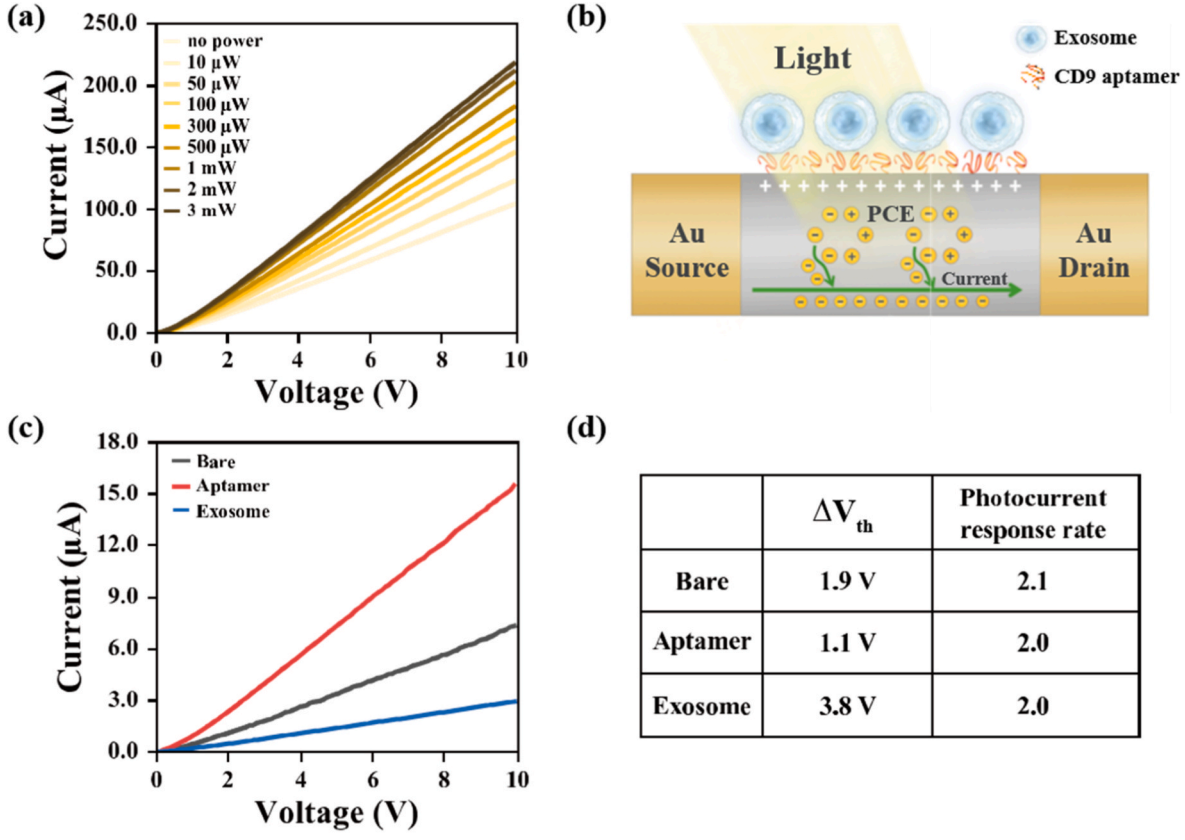
The surface parameters of the constructed biosensing structures corresponding to Fig. 2b, c and 2d are summarized in Fig. 2e. Although the vertical distance and image-based observations provided a visual representation of the immobilization stages, the quantitatively quantified data further validated these findings. The average roughness (Ra) quantifies the overall surface texture based on the arithmetic mean of absolute deviations, whereas the root mean square roughness (Rq) is more sensitive to pronounced variations such as surface protrusions and depressions [44]. As a result, Rq can reveal surface characteristics that may not be captured by Ra alone. The inclusion of both parameters allows for a more robust interpretation of topographical and functional surface properties. Compared to the Rq and Ra values of the ReS_2 surface, which were measured to be approximately 1.029 ± 0.169 nm and 0.870 ± 0.172 nm, respectively, the enormous increases in surface roughness across the immobilization steps confirmed the successful construction of the sensing structure.

3.2. *Electrical signal and stability analysis of ReS_2-based L-FET platform*

The physical behavior and signal stability of the fabricated ReS_2-based L-FET were investigated under varying illumination conditions to assess its suitability for biosensing applications. The signal behavior was measured in a ReS_2 device without biomolecular binding under varying levels of illumination power (Fig. 3a). As expected, the signal amplification owing to photo-generated carrier formation was evident under the PCE; however, after reaching a certain level of illumination, a saturation point was observed, which resulted in diminished signal amplification. This saturation effect showed that the concentration of photo-generated carriers produced by illumination eventually reached a limit, leading to a plateau in the signal amplification.

The physical behavior of the carriers under incident light on the transferred ReS_2 surface is shown in Fig. 3b. When focused light was applied to the ReS_2 channel, bound electrons were excited, and holes were generated, initiating the PCE. Photo-generated carriers were excited to the conduction band when the incident energy exceeded the energy bandgap of the material, resulting in the amplification of the photodetection signal. Additionally, light absorption enhanced the conductivity of the ReS_2, subsequently increasing the current density within the channel.

Thus, the illumination power affected both the carrier concentration



	ΔV_{th}	Photocurrent response rate
Bare	1.9 V	2.1
Aptamer	1.1 V	2.0
Exosome	3.8 V	2.0

Fig. 3. Data illustrating the physical behavior of the L-FET device. (a) I-V curve trends of the L-FET device under varying illumination power levels. (b) Schematic showing carrier behavior under applied illumination power. (c) I-V curve trends following the deposition of the sensing structure. (d) Table displaying threshold voltage shifts and bright/dark ratio under different sensing structures.

and conductivity, leading to signal amplification in the fabricated biosensor [45]. As the biomolecules were integrated into the fabricated sensor, signal variations were evident (Fig. 3c). Following aptamer immobilization, an initial signal increase of approximately two orders of magnitude is detected, attributable to the negative charge introduced to the ReS_2 channel surface by the phosphate groups of the aptamer. This created the negatively charged regions, making it easier for the photo-generated holes to migrate to the ReS_2 channel surface. Consequently, current-signal amplification could be observed. Upon exosome binding to the immobilized aptamer, a pronounced decrease in the signal was evident. This trend suggested a potential interaction between the exosomes and the sensor surface; however, the exact cause of this decrease requires further investigation in the future.

A threshold voltage (V_{th}) was defined as the point at which the current signal exceeded 10^{-6} A, and changes in V_{th} and the bright/dark ratio were analyzed across each step of the sensing structure (Fig. 3d). The surface charge introduced by the phosphate groups of the aptamer acted as a local gate at the ReS_2 interface, causing a negative shift in V_{th}. Following the binding of the exosomes to the immobilized aptamer, a substantial positive shift in V_{th} could be observed. However, the mechanisms underlying this response remain unclear and require further investigation. The signal amplification driven by the PCE is represented by the bright/dark ratio. This amplification ratio was determined by comparing the current measured under illumination with a maximum laser power of 3 mW to that obtained under dark (no laser) conditions. Specifically, the comparison was made using the current value at the highest applied voltage (i.e., the end point of the I–V curve), and the resulting value was calculated as a relative ratio. This turn-on/turn-off ratio approach was consistently applied across all device functionalization stages, including the bare, aptamer-modified, and exosome-bound states. This analysis suggests that, similar to how dopants in pure semiconductor increase concentration of carriers, photo-generated carriers may lead to increase in channel current. Accordingly, in the fabricated L-FET device, the amplification ratio under light exposure increased by approximately twofold, indicating a substantial enhancement in signal response.

A comparison of the signal performance was also conducted with MoS_2, a material known for its high carrier mobility and photosensitivity, commonly used as a photodetector channel in optoelectronic applications [46]. After applying illumination powers of 100, 500, and 1000 μW, the increased signals were expressed as ΔI and plotted as a function of the sweep voltage (Fig. S3a). As expected, the MoS_2 exhibited higher signals and ΔI compared to the ReS_2, consistent with its known properties of superior electron mobility and photosensitivity [47]. To assess the signal variability between the devices, a signal comparison was conducted across eight randomly selected substrates (Fig. S3b). Whereas the ReS_2 devices exhibited relatively stable signals around the 2 μA range, the MoS_2 exhibited considerably more variability in signal across different substrates, with higher signal deviations. This variability could be attributed to the differences in the size and thickness of the 2D materials exfoliated mechanically for each substrate, as layer thickness inconsistencies inevitably lead to signal variations between the devices. TMD possess an intrinsically layered two-dimensional structure, wherein individual atomic layers are sequentially stacked as the material thickness increases. Within such stacked architectures, interlayer van der Waals interactions play a pivotal role in modulating both physical and electronic properties [48]. Notably, the bandgap of conventional TMDs is highly sensitive to the strength of interlayer coupling, often exhibiting substantial variations as a function of thickness. Nevertheless, ReS_2 exhibits exceptionally weak interlayer coupling, enabling it to retain electronic behavior to those of a monolayer even in its bulk form. This unique feature renders ReS_2 largely insensitive to thickness-dependent modifications in its electronic structure, thereby resulting in a nearly thickness-independent bandgap profile [49]. Consequently, the relative signal stability of ReS_2 compared to MoS_2 makes it a more suitable candidate for biosensor applications.

3.3. Optimization of sensing structure conditions for electrical signal measurement

The optimization of the illumination power for application to biomolecules was evaluated by monitoring the signal variations at different laser intensities (Fig. 4a). Upon immobilizing the aptamer at a concentration of 100 nM, signal changes were measured under illumination at various intensities for 5 min. As the illumination power increased, a corresponding signal increase could be observed, which was consistent with the general device trends. However, at power outputs above approximately 500 μW, a decrease in signal was detected. This decline could be attributed to physical damage to biomolecules, which increased the resistance to illumination.

Adipocyte-derived exosomes were added at a concentration of 10^7 exosomes/mL under identical conditions (Fig. 4b). Unlike the aptamer, the exosome target acted as a resistive element, resulting in a lower absolute signal than that illustrated in Fig. 4a. However, an increase in the signal owing to photo-generated carrier amplification was still evident. Like the aptamer, a sharp signal drop occurred at illumination powers exceeding 500 μW, indicating that the resistance from the damaged sample surpassed that of the exosomes within the channel. Consequently, a maximum illumination power of 400 μW which did not damage the biomolecules was selected as the standard for signal measurements in this study. Before performing the performance evaluations, the optimal concentrations of the aptamer and exosomes were determined at the reference laser intensity using the same method (Fig. 4c and d). For the aptamer, the signal increase compared to the bare signal was evaluated across a range of concentrations from 100 pM to 1 μM, with the greatest signal amplification being observed at 10 nM. Contrary to the expectation that higher aptamer concentrations would lead to a larger signal increase owing to the accumulation of negative charges, the results demonstrated that increased resistance from local aptamer aggregation led to a diminished signal increase.

For the exosomes, a considerable reduction in the signal was evident across the entire concentration range. However, at a concentration of approximately 10 exosomes/mL, little or no signal change could be detected. Meaningful signal variations were observed, starting at a concentration of 10^2 exosomes/mL, indicating that the optimal conditions for detection were 10 nM aptamer and exosome concentrations above 10^2 exosomes/mL. Consequently, these conditions were used to calculate the detection limits.

3.4. Performance evaluation of CD9 protein detection in fabricated L-FET platform

To evaluate the detection performance of the L-FET platform for CD9 protein within exosomes, I-V and ΔI measurements were conducted across a range of preadipocyte exosome concentrations diluted in DIW, as illustrated in Fig. 5a and b. The current-voltage (I-V) curves exhibited a negative correlation that is, the signal decreased with increasing exosome concentration, owing to increased resistance. Conversely, ΔI exhibited a positive correlation that is, the increase in ΔI was linearly proportional to the logarithmic concentration of exosomes over the dynamic range of 10^2–10^7 exosomes/mL. At 10 V, the ΔI values were 6.57, 5.62, 4.68, 1.94, and 0.35 μA, respectively. The regression equation for the calibration curve was determined to be $y = 0.153 \log[\text{exosomes}] - 4.16$, with an R^2 value of 0.99. The LOD was calculated to be 5.94×10^2 exosomes/mL by applying 3.3 (standard deviation/slope), as referenced from previous studies [50–52].

The signal reduction evident in the I-V curves followed a trend similar to that observed in the buffer condition; however, the extent of reduction was lower, owing to the presence of various interfering substances in the serum, which could have reduced the reactivity of the sensor [53,54] (Fig. 5c and d). The measured ΔI values in serum were 1.43, 0.93, 0.61, and 0.09 μA, exhibiting a slight reduction compared to those in the DIW. The regression equation and R^2 value were $y =$

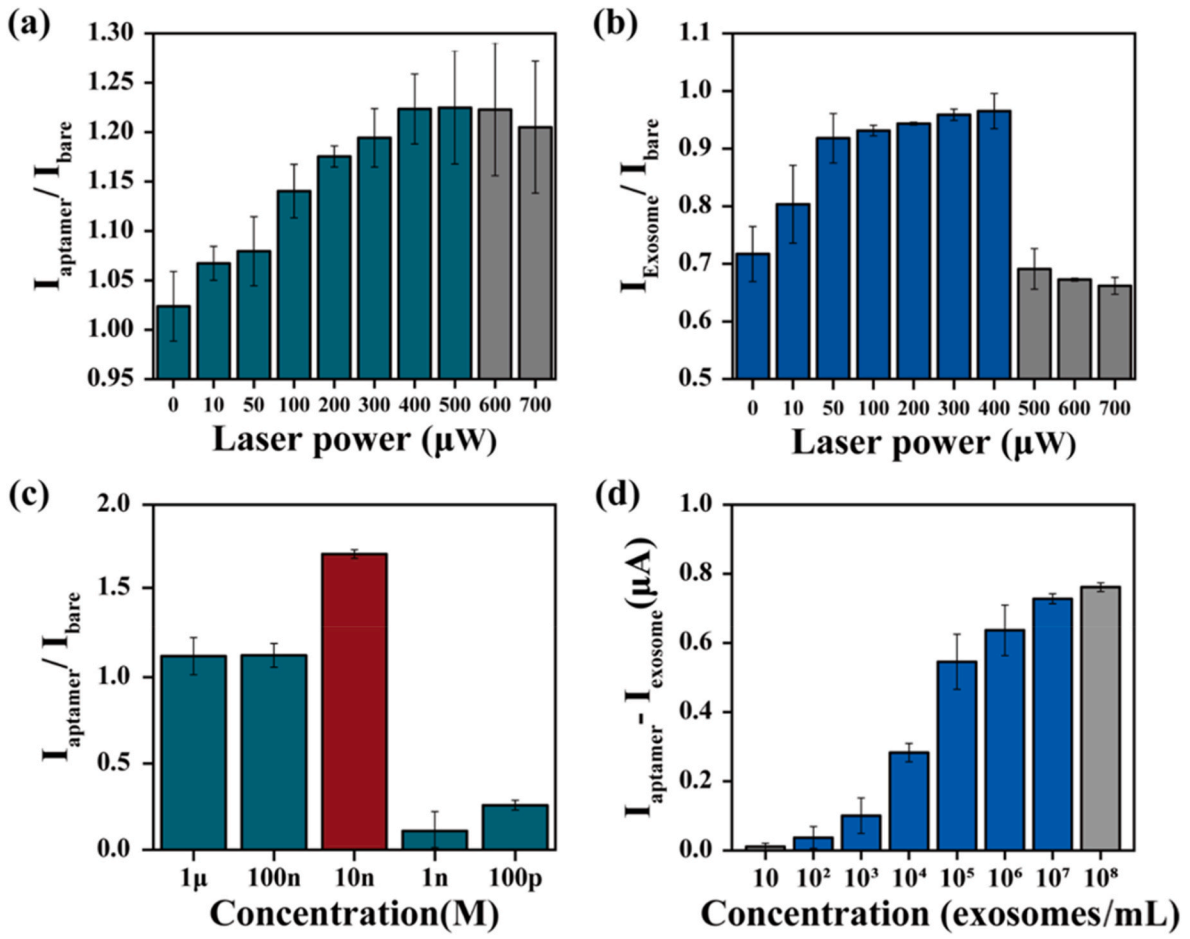


Fig. 4. Data demonstrating signal optimization. (a) Signal variation graph as a function of illumination power intensity after aptamer conjugation. (b) Signal variation graph as a function of illumination power intensity after aptamer-exosome binding. (c) Signal variation graph for aptamer concentration optimization. (d) Signal variation graph for exosome concentration range determination.

0.44257 log[exosomes] – 1.65969, and 0.99, respectively, with a detection limit of 9.79 × 10^3 exosomes/mL. These values demonstrated a superior detection range and LOD compared to those of previous studies targeting the CD9 protein (Table 1).

These results demonstrated that the signal amplification strategy using photo-generated carriers was effective for detecting low-concentration samples and confirmed that stable detection was achievable even when the sensor circuit was directly interfaced with biological materials. Consequently, the fabricated L-FET biosensor could be effectively applied as a platform for exosome detection.

4. Conclusions

The L-FET platform was the first model that integrated the direct circuit coupling of biological materials with semiconductor devices while implementing a FET structure via illumination power. The signal amplification mechanism of the photo-generated carriers, driven by the PCE, provides effective performance for detecting low-concentration biomolecules, whereas the structural simplification ensured ease of fabrication and offered an excellent strategy for biosensor miniaturization. Furthermore, the platform eliminates the need for gate/oxide structures through a light-driven mechanism, highlighting a novel from of signal control in biosensing applications. By leveraging the direct bandgap of the ReS_2 channel, this platform minimized signal variability between substrates, thereby establishing a biosensor with high reproducibility and stability.

With the proposed platform, optimized measurement conditions using illumination power of 400 μW enabled the detection of human preadipocyte exosomes. A detection limit of 4.4 × 10^2 exosomes/mL was achieved under DIW conditions, and a detection limit of 9.79 × 10^3 exosomes/mL was obtained in 10 % human serum. Compared to conventional detection methods, this platform provided superior sensitivity and a broader detection range, considerably expanding its potential for early diagnosis applications.

Consequently, the L-FET platform, as the first photodetector model to directly combine biological molecules and semiconductors, demonstrated commercial potential through its signal amplification strategy using photo-generated carriers and structural simplification. Moreover, owing to its low detection limit and wide detection range, the platform proved to be a practical and reliable tool for detecting various biomarkers, including the CD9 protein. This suggests that the proposed platform could serve as an innovative solution for early diagnostic systems targeting emerging pathogens in future clinical settings.

CRediT authorship contribution statement

Moonbong Jang: Investigation. **Woongki Na:** Methodology. **Minyoung Lee:** Investigation. **Seokho Jung:** Investigation. **Yeeun Woo:** Investigation. **Hah Young Yoo:** Conceptualization. **Taek Lee:** Writing – original draft, Conceptualization. **Junhong Min:** Writing – review & editing, Supervision.

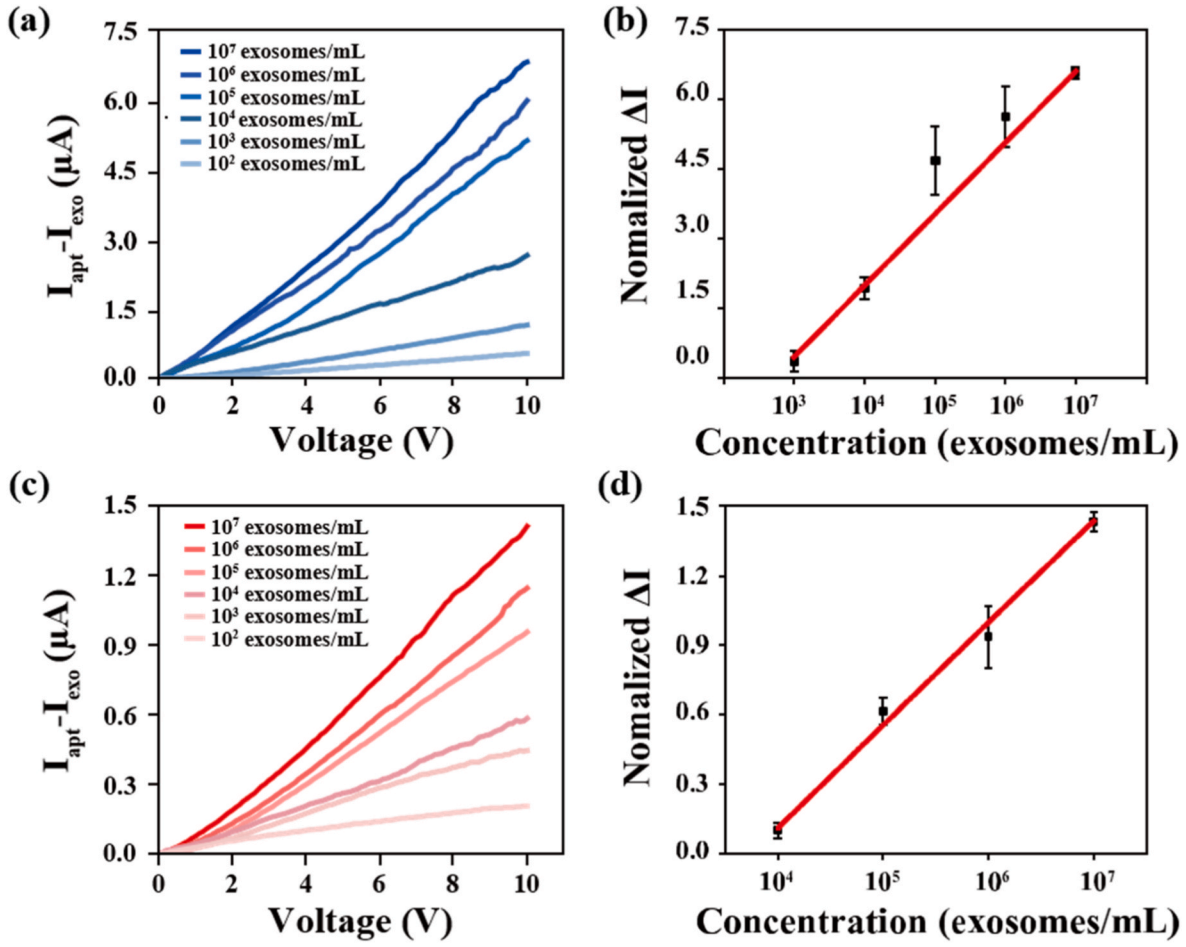


Fig. 5. (a) I-V graphs at various concentrations of preadipocyte exosomes diluted in deionized water (DIW) (concentration range: 10^2–10^7 exosomes/mL). (b) Linear regression curves for various concentrations of preadipocyte exosomes diluted in DIW. (c) I-V graphs at various concentrations of preadipocyte exosomes diluted in 10 % human serum (concentration range: 10^2–10^7 exosomes/mL). (d) Linear regression curves for various concentrations of preadipocyte exosomes diluted in 10 % human serum.

Table 1
Antibody and aptamer-based biosensors for exosome detection.

Target	Probe	Detection method	Detection range (exosomes/mL)	LOD (exosomes/mL)	Ref.
Breast cancer exosome	Antibody	EIS, CV	5.0×10^2–5.0×10^5	166	[56]
HepG2 exosome	Aptamer	SPR	1.0×10^6–1.0×10^9	1.0×10^6	[57]
Fetal bovine exosome	Antibody	ELISA	1.0×10^5–1.0×10^9	2.0×10^5	[58]
Breast cancer exosome	Antibody	SWV	1.0×10^8–3.0×10^{12}	1.0×10^8	[59]
HepG2 exosome	Antibody	FET	3.3×10^4–3.3×10^9	3.4×10^4	[60]
Cord blood exosome	Aptamer	FET	1.0×10^3–1.0×10^7	6.4×10^2	[61]
HepG2 exosome	Antibody	FET	3.3×10^4–3.3×10^9	7.3×10^3	[62]
Ovarian cancer exosome	Antibody	Optical	1.0×10^8–1.0×10^9	117.9×10^6	[63]
Human preadipocyte exosome	Aptamer	L-FET	1.0×10^4–1.0×10^7	6.05×10^3	This study

Declaration of competing interest

The authors declare that they have no known competing financial interests or personal relationships that could have appeared to influence the work reported in this paper.

Acknowledgements

This work was supported by the Materials & Components Technology Development Program (RS-2024-00507931, The development of multiplex array diagnostic materials and pretreatment modules for analyzing inflammatory diseases in the elderly) funded By the Ministry of Trade Industry & Energy(MOTIE, Korea) and by the National Research Foundation of Korea(NRF) grant funded by the Korea government(MSIT) (RS-2024-00416117) and by Research Program funded by the National Research Council of Science & Technology(NST), (CRC22024-200).

Appendix A. Supplementary data

Supplementary data to this article can be found online at https://doi.org/10.1016/j.mtbio.2025.102281.

Data availability

No data was used for the research described in the article.

References

[1] D. Wang, S. Yang, N. Wang, H. Guo, S. Feng, Y. Luo, J. Zhao, A novel microfluidic strategy for efficient exosome separation via thermally oxidized non-uniform deterministic lateral displacement (DLD) arrays and dielectrophoresis (DEP) synergy, Biosensors 14 (4) (2024) 174.

[2] D. Bhavsar, R. Raguraman, D. Kim, X. Ren, A. Munshi, K. Moore, R. Ramesh, Exosomes in diagnostic and therapeutic applications of ovarian cancer, J. Ovarian Res. 17 (1) (2024) 113.

[3] A. Kowalczyk, A. Gajda-Walczak, M. Ruzycka-Ayoush, A. Targonska, G. Mosieniak, M. Glogowski, I.P. Grudzinski, Parallel SPR and QCM-D quantitative analysis of CD9, CD63, and CD81 tetraspanins: a simple and sensitive way to determine the concentration of extracellular vesicles isolated from human lung cancer cells, Anal. Chem. 95 (25) (2023) 9520–9530.

[4] N. Yunusova, E. Dzhugashvili, A. Yalovaya, L. Kolomiets, A. Shefer, A. Grigor'eva, S. Tamkovich, Comparative analysis of tumor-associated microRNAs and tetraspanines from exosomes of plasma and ascitic fluids of ovarian cancer patients, Int. J. Mol. Sci. 24 (1) (2022) 464.

[5] X. Han, W.H. Zhang, H.L. Gao, T.J. Li, H.X. Xu, H. Li, L. Liu, Neoadjuvant chemotherapy endows CD9 with prognostic value that differs between tumor and stromal areas in patients with pancreatic cancer, J. Clin. Lab. Anal. 36 (7) (2022) e24517.

[6] M.I. Mustafa, A.M. Makhawi, SHERLOCK and DETECTR: CRISPR-Cas systems as potential rapid diagnostic tools for emerging infectious diseases, J. Clin. Microbiol. 59 (3) (2021) 10–1128, https://doi.org/10.1128/jcm.00745-20.

[7] M. Ghaderzadeh, F. Asadi, Deep learning in the detection and diagnosis of COVID-19 using radiology modalities: a systematic review, J. Healthc. Eng. 2021 (1) (2021) 6677314, https://doi.org/10.1155/2021/6677314.

[8] J. Choe, J. Kim, H.H. Kwon, H. Hong, C.Y. Jung, C. Jeon, E. Park, S. Kim, Diagnostic performance of immunochromatography assay for rapid detection of IgM and IgG in coronavirus disease 2019, J. Med. Virol. 92 (11) (2020) 2567–2572, https://doi.org/10.1002/jmv.26060.

[9] M. Teymouri, S. Mollazadeh, H. Mortazavi, Z.N. Ghale-Noie, V. Keyvani, F. Aghababaei, M.R. Hamblin, G. Abbaszadeh-Goudarzi, H. Pourghadamyari, S.M. R. Hashemian, Recent advances and challenges of RT-PCR tests for the diagnosis of COVID-19, Pathol. Pract. 221 (2021) 153443, https://doi.org/10.1016/j.prp.2021.153443.

[10] F. Gallivanone, G. Bertoli, D. Radiogenomics Porro, Breast cancer diagnosis and characterization: current status and future directions, Methods Protoc. 5 (5) (2022) 78, https://doi.org/10.3390/mps5050078.

[11] M.M. Ahsan, S.A. Luna, Z. Siddique, Machine-learning-based disease diagnosis: a comprehensive review, in: Healthcare, vol. 10, MDPI, 2022, p. 541, https://doi.org/10.3390/healthcare10030541.

[12] B.M. Rashed, N. Popescu, Critical analysis of the current medical image-based processing techniques for automatic disease evaluation: systematic literature review, Sensors 22 (18) (2022) 7065, https://doi.org/10.3390/s22187065.

[13] M. Mirbabaie, S. Stieglitz, N.R.J. Frick, Artificial intelligence in disease diagnostics: a critical review and classification on the current state of research guiding future direction, Health Technol. 11 (4) (2021) 693–731, https://doi.org/10.3390/s22187065.

[14] N. Ghaffar Nia, E. Kaplanoglu, A. Nasab, Evaluation of artificial intelligence techniques in disease diagnosis and prediction, Discov. Artif. Intell. 3 (1) (2023) 5, https://doi.org/10.1007/s44163-023-00049-5.

[15] A. Haleem, M. Javaid, R.P. Singh, R. Suman, S. Rab, Biosensors applications in medical field: a brief review, Sens. Int. 2 (2021) 100100, https://doi.org/10.1016/j.sintl.2021.100100.

[16] I. Palchetti, M. Mascini, Biosensor Technology: a brief history, in: Sensors and Microsystems: AISEM 2009 Proceedings, Springer, 2009, pp. 15–23, https://doi.org/10.1007/978-90-481-3606-3_2.

[17] A. Khan, E. DeVoe, S. Andreescu, Carbon-based electrochemical biosensors as diagnostic platforms for connected decentralized healthcare, Sensors & Diagnostics 2 (3) (2023) 529–558, https://doi.org/10.1039/D2SD00226D.

[18] L.C. Brazaca, P.L. Dos Santos, P.R. de Oliveira, D.P. Rocha, J.S. Stefano, C. Kalinke, R.A.A. Munoz, J.A. Bonacin, B.C. Janegitz, E. Carrilho, Biosensing strategies for the electrochemical detection of viruses and viral diseases–A review, Anal. Chim. Acta 1159 (2021) 338384, https://doi.org/10.1016/j.aca.2021.338384.

[19] Y. Yoon, Y. Kwon, H. Park, S. Lee, C. Park, T. Lee, Recent progress in rapid biosensor fabrication methods: focus on electrical potential application, BioChip J. 18 (1) (2024) 1–21, https://doi.org/10.1007/s13206-023-00127-x.

[20] J.A. Park, Y. Seo, H. Sohn, C. Park, J. Min, T. Lee, Recent trends in biosensors based on electrochemical and optical techniques for cyanobacterial neurotoxin detection, BioChip J 16 (2) (2022) 146–157, https://doi.org/10.1007/s13206-022-00054-3.

[21] D. Chowdhury, B.P. De, B. Appasani, N.K. Singh, R. Kar, D. Mandal, N. Bizon, P. Thounthong, A novel dielectric modulated gate-stack double-gate metal-oxide-semiconductor field-effect transistor-based sensor for detecting biomolecules, Sensors 23 (6) (2023) 2953, https://doi.org/10.3390/s23062953.

[22] T. Wadhera, D. Kakkar, G. WadhFwa, B. Raj, Recent advances and progress in development of the field effect transistor biosensor: a review, J. Electron. Mater. 48 (2019) 7635–7646, https://doi.org/10.1007/s11664-019-07705-6.

[23] M. Sedki, Y. Shen, A. Mulchandani, Nano-FET-enabled biosensors: materials perspective and recent advances in north America, Biosens. Bioelectron. 176 (2021) 112941, https://doi.org/10.1016/j.bios.2020.112941.

[24] M.T. Amen, T.T.T. Pham, E. Cheah, D.P. Tran, B. Thierry, Metal-oxide FET biosensor for point-of-care testing: overview and perspective, Molecules 27 (22) (2022) 7952, https://doi.org/10.3390/molecules27227952.

[25] M. Rahman, K. Davey, S. Qiao, Advent of 2D rhenium disulfide (ReS_2): fundamentals to applications, Adv. Funct. Mater. 27 (10) (2017) 1606129, https://doi.org/10.1002/adfm.201606129.

[26] Y.-C. Lin, H.-P. Komsa, C.-H. Yeh, T. Bjorkman, Z.-Y. Liang, C.-H. Ho, Y.-S. Huang, P.-W. Chiu, A.V. Krasheninnikov, K. Suenaga, Single-layer ReS_2: two-dimensional semiconductor with tunable in-plane anisotropy, ACS Nano 9 (11) (2015) 11249–11257, https://doi.org/10.1021/acsnano.5b04851.

[27] E. Gibney, The super materials that could trump graphene, Nature 522 (7556) (2015), https://doi.org/10.1038/522274a.

[28] T. Chowdhury, E.C. Sadler, T.J. Kempa, Progress and prospects in transition-metal dichalcogenide research beyond 2D, Chem. Rev. 120 (22) (2020) 12563–12591, https://doi.org/10.1021/acs.chemrev.0c00505.

[29] J. Lu, H. Liu, E.S. Tok, C.-H. Sow, Interactions between lasers and two-dimensional transition metal dichalcogenides, Chem. Soc. Rev. 45 (9) (2016) 2494–2515, https://doi.org/10.1039/C5CS00553A.

[30] E. Liu, Y. Fu, Y. Wang, Y. Feng, H. Liu, X. Wan, W. Zhou, B. Wang, L. Shao, C.-H. Ho, Integrated digital inverters based on two-dimensional anisotropic ReS_2 field-effect transistors, Nat. Commun. 6 (1) (2015) 1–7, https://doi.org/10.1038/ncomms7991.

[31] B. Peng, P.K. Ang, K.P. Loh, Two-dimensional dichalcogenides for light-harvesting applications, Nano Today 10 (2) (2015) 128–137, https://doi.org/10.1016/j.nantod.2015.01.007.

[32] X. Tong, E. Ashalley, F. Lin, H. Li, Z.M. Wang, Advances in MoS_2-based field effect transistors (FETs), Nano-Micro Lett. 7 (2015) 203–218, https://doi.org/10.1007/s40820-015-0034-8.

[33] D. Kufer, G. Konstantatos, Photo-FETs: phototransistors enabled by 2D and 0D nanomaterials, Acs Photonics 3 (12) (2016) 2197–2210, https://doi.org/10.1021/acsphotonics.6b00391.

[34] P. Bergveld, Thirty years of ISFETOLOGY: what happened in the past 30 Years and what may happen in the next 30 years, Sensor. Actuator. B Chem. 88 (1) (2003) 1–20, https://doi.org/10.1016/S0925-4005(02)00301-5.

[35] P. Bergveld, The development and application of FET-based biosensors, Biosensors 2 (1) (1986) 15–33, https://doi.org/10.1016/0265-928X(86)85010-6.

[36] H.-S. Wong, M.H. White, A CMOS-Integrated'ISFET-operational amplifier'chemical sensor employing differential sensing, IEEE Trans. Electron. Dev. 36 (3) (1989) 479–487, https://doi.org/10.1109/16.19957.

[37] J. Janata, Electrochemical microsensors, Proc. IEEE 91 (6) (2003) 864–869, https://doi.org/10.1109/JPROC.2003.813576.

[38] B. Jariwala, D. Voiry, A. Jindal, B.A. Chalke, R. Bapat, A. Thamizhavel, M. Chhowalla, M. Deshmukh, A. Bhattacharya, Synthesis and Characterization of ReS_2 and $ReSe_2$ Layered Chalcogenide Single Crystals, Chem. Mater. 28 (10) (2016) 3352–3359, https://doi.org/10.1021/acs.chemmater.6b00364.

[39] J. Yoon, J. Lim, M. Shin, T. Lee, J.-W. Choi, Toward bioelectronic device based on bionanohybrid composed of nanomaterials and biomaterials: from nucleic acid and protein to living cell, Appl. Phys. Rev. 10 (1) (2023), https://doi.org/10.1063/5.0116714.

[40] M. Lee, S.J. Park, G. Kim, C. Park, M.-H. Lee, J.-H. Ahn, T. Lee, A pretreatment-free electrical capacitance biosensor for exosome detection in undiluted serum, Biosens. Bioelectron. 199 (2022) 113872, https://doi.org/10.1016/j.bios.2021.113872.

[41] Q. Ren, L. Ga, Z. Lu, J. Ai, T. Wang, Aptamer-functionalized nanomaterials for biological applications, Mater. Chem. Front. 4 (6) (2020) 1569–1585, https://doi.org/10.1039/C9QM00779B.

[42] M. Jang, M. Lee, H. Sohn, C. Park, T. Lee, Fabrication of rapid electrical pulse-based biosensor consisting of truncated DNA aptamer for zika virus envelope protein detection in clinical samples, Materials 16 (6) (2023) 2355, https://doi.org/10.3390/ma16062355.

[43] M.O. Ershova, A. Taldaev, P.V. Konarev, G.S. Peters, A.A. Valueva, I.A. Ivanova, T. O. Pleshakova, Selection of aptamers for use as molecular probes in AFM detection of proteins, Biomolecules 13 (12) (2023) 1776.

[44] R.T. Mushtaq, A. Iqbal, Y. Wang, Q. Cheok, S. Abbas, Parametric effects of fused filament fabrication approach on surface roughness of acrylonitrile butadiene styrene and nylon-6 polymer, Materials 15 (15) (2022) 5206.

[45] I. Chahardah Cherik, S. Mohammadi, Fringe-fields-modulated double-gate tunnel-FET biosensor, Sci. Rep. 14 (1) (2024) 168, https://doi.org/10.1038/s41598-023-50723-y.

[46] A. Taffelli, S. Dirè, A. Quaranta, L. Pancheri, MoS_2 based photodetectors: a review, Sensors 21 (8) (2021) 2758, https://doi.org/10.3390/s21082758.

[47] R. Nur, T. Tsuchiya, K. Toprasertpong, K. Terabe, S. Takagi, M. Takenaka, High responsivity in MoS_2 phototransistors based on charge trapping HfO_2 dielectrics, Commun. Mater. 1 (1) (2020) 103, https://doi.org/10.1038/s43246-020-00103-0.

[48] C. Cho, J. Wong, A. Taqieddin, S. Biswas, N.R. Aluru, S. Nam, H.A. Atwater, Highly strain-tunable interlayer excitons in MoS_2/WSe_2 heterobilayers, Nano Lett. 21 (9) (2021) 3956–3964.

[49] E. Zhang, Y. Jin, X. Yuan, W. Wang, C. Zhang, L. Tang, S. Liu, P. Zhou, W. Hu, F. Xiu, ReS_2-based field-effect transistors and photodetectors, Adv. Funct. Mater. 25 (26) (2015) 4076–4082, https://doi.org/10.1002/adfm.201500969.

[50] C. Nico, T.C. Bakker Schut, P.J. Caspers, G.J. Puppels, Limits of detection of topically applied products in the skin using in vivo Raman spectroscopy, Pharmaceutics 16 (3) (2024) 304.

[51] F. Poggialini, S. Legnaioli, B. Campanella, B. Cocciaro, G. Lorenzetti, S. Raneri, V. Palleschi, Calculating the limits of detection in laser-induced breakdown spectroscopy: not as easy as it might seem, Appl. Sci. 13 (6) (2023) 3642.

[52] Y. Yoon, C. Baek, D. Yoo, Y. Seo, S. Lee, S.W. Shin, T. Lee, Construction of on-site DNA pre-treatment device and rapid electrochemical biosensor set for Escherichia coli detection in milk, Chem. Eng. J. 499 (2024) 155898.

[53] G. Park, H. Lee, M. Jang, J.A. Park, H. Park, C. Park, T. Lee, Rapid electrical biosensor consisting of DNA aptamer/carbon nanonetwork on microelectrode array for cardiac troponin I in human serum, Sensors and Actuators B: Chemical. 393 (2023) 134295.
[54] H. Park, H. Lee, M. Lee, C. Baek, J.A. Park, M. Jang, Y. Kwon, J. Min, T. Lee, Synthesis of isolated DNA aptamer and its application of AC-electrothermal flow based rapid biosensor for detection of dengue virus in spiked sample, Bioconju. Chem. 34 (8) (2023) 1486.
[55] D. Murase, K. Shinokita, Y. Wakafuji, M. Onodera, T. Machida, K. Watanabe, K. Matsuda, All dry transfer processes utilizing Au exfoliation for predetermined shapes of transition metal dichalcogenide, Langmuir 41 (16) (2025) 10099–10107.
[56] X. Chen, X. Yan, J. Qiu, X. Zhang, Y. Zhang, H. Zhou, Y. Zhao, L. Han, Y. Zhang, An RGO-doped laser induced graphene electrochemical biosensor for highly sensitive exosome detection, Sensors & Diagnostics (2024), https://doi.org/10.1039/D4SD00181H.
[57] Q. Zhou, A. Rahimian, K. Son, D.-S. Shin, T. Patel, A. Revzin, Development of an aptasensor for electrochemical detection of exosomes, Methods 97 (2016) 88–93, https://doi.org/10.1016/j.ymeth.2015.10.012.
[58] X. Doldán, P. Fagúndez, A. Cayota, J. Laíz, J.P. Tosar, Electrochemical sandwich immunosensor for determination of exosomes based on surface marker-mediated signal amplification, Anal. Chem. 88 (21) (2016) 10466–10473, https://doi.org/10.1021/acs.analchem.6b02421.
[59] S. Yadav, K. Boriachek, M.N. Islam, R. Lobb, A. Möller, M.M. Hill, M. S. Al Hossain, N. Nguyen, M.J.A. Shiddiky, An electrochemical method for the detection of disease-specific exosomes, Chemelectrochem 4 (4) (2017) 967–971, https://doi.org/10.1002/celc.201600391.
[60] Y. Yu, Y.-T. Li, D. Jin, F. Yang, D. Wu, M.-M. Xiao, H. Zhang, Z.-Y. Zhang, G.-J. Zhang, Electrical and label-free quantification of exosomes with a reduced graphene oxide field effect transistor biosensor, Anal. Chem. 91 (16) (2019) 10679–10686, https://doi.org/10.1021/acs.analchem.9b01950.
[61] J. An, H. Park, J. Kim, H. Park, T.-H. Kim, C. Park, J. Kim, M.-H. Lee, T. Lee, Extended-gate field-effect transistor consisted of a CD9 aptamer and MXene for exosome detection in human serum, ACS Sens. 8 (8) (2023) 3174–3186, https://doi.org/10.1021/acssensors.3c00879.
[62] C. Wang, D. Jin, Y. Yu, L. Tang, Y. Sun, Z. Sun, G.-J. Zhang, A dual antibody-modified nanochannel biosensor for capture and identification of exosomes, Sensor. Actuator. B Chem. 314 (2020) 128056, https://doi.org/10.1016/j.snb.2020.128056.
[63] Z. Chen, Q. Liang, H. Zeng, Q. Zhao, Z. Guo, R. Zhong, M. Xie, X. Cai, J. Su, Z. He, Exosomal CA125 as a promising biomarker for ovarian cancer diagnosis, J. Cancer 11 (21) (2020) 6445, https://doi.org/10.7150/jca.48531.